Nonedge-Specific Adaptive Scheme for Highly Robust Blind Motion Deblurring of Natural Imagess

Chao Wang, Yong Yue, Feng Dong, Yubo Tao, Xiangyin Ma, Gordon Clapworthy, Hai Lin, and Xujiong Ye

***Abstract*— Blind motion deblurring estimates a sharp image from a motion blurred image without the knowledge of the blur kernel. Although significant progress has been made on tackling this problem, existing methods, when applied to highly diverse natural images, are still far from stable. This paper focuses on the robustness of blind motion deblurring methods toward image diversity—a critical problem that has been previously neglected for years. We classify the existing methods into two schemes and analyze their robustness using an image set consisting of 1.2 million natural images. The first scheme is edge-specific, as it relies on the detection and prediction of large-scale step edges. This scheme is sensitive to the diversity of the image edges in natural images. The second scheme is nonedge-specific and explores various image statistics, such as the prior distributions. This scheme is sensitive to statistical variation over different images. Based on the analysis, we address the robustness by proposing a novel nonedge-specific adaptive scheme (NEAS), which features a new prior that is adaptive to the variety of textures in natural images. By comparing the performance of NEAS against the existing methods on a very large image set, we demonstrate its advance beyond the state-of-the-art.**

***Index Terms*— Blind deconvolution, image restoration, maximum a posteriori estimation.**

I. Introduction

RECOVERING a sharp image from a motion blurred image without the knowledge of its blur kernel is called blind motion deblurring. This is an interesting problem in many applications, including video surveillance, medical imaging and consumer photography, to name but a few.

One of the critical challenges of blind motion deblurring is that it is severely ill-posed - the number of unknowns is much greater than the number of available measurements. Given a blurred image, we need to work out its sharp version and the blur kernel. Although significant progress has been made in the last few years [1]–[15], the latest techniques are still not very robust, especially in the face of highly diverse natural images. Most of the existing methods have been tested only on very small sets of natural images. In fact, some algorithms are able to produce satisfactory results only on a small number of selected images. The poor robustness has severely hindered the applicability of the deblurring techniques to real-world applications.

Since many aspects of blind motion deblurring have remained unclear until recently [16]–[18], technical robustness to highly diverse natural images has not yet received sufficient attention within the image processing community. This work is designed to address the robustness issue by revealing the key principles associated with the robustness of blind motion deblurring to extremely diverse natural images. An in-depth analysis of recent techniques has been carried out, both experimentally and theoretically, based on which a novel method is proposed; this has been found to outperform the existing methods. Notably, the analysis and evaluation has involved the use of 1.2 million natural images from ImageNet [19].

It was generally considered that the image sparse derivative prior favored natural images. The sparse derivative prior suggests that the distribution of gradients in natural images is sharply peaked at zero and relatively heavy-tailed, which deviates greatly from standard Gaussian distributions. However, Levin et al. [16] found that the sparse prior actually favors blurred images instead of the latent sharp one, which makes the classical maximum-a-posteriori (MAP) estimation produce a dense kernel, rather than the true kernel [16].

We categorize existing methods into edge-specific and non-edge specific schemes.

The edge-specific scheme relies on the efficient **detection** or **prediction** of large-scale step edges (LSEDs) [11], [13], [15], [17], [18], [20]–[22].

1) Detection-based methods [11], [13], [15], [20] assume that sharp explanations (i.e., the sharp version of an input blurred image) are favored by the sparse prior for LSEDs. In other words, the detection of LSEDs can lead to the generation of a sharp version of the input blurred image. However, as will be shown in this paper, this assumption holds only at a few small windows around the LSEDs. This fails to guarantee robust kernel estimation.
2) Prediction-based methods adopt sharpening filters [17], [18], [21], [23] or the inverse Radon transform [22] to

Manuscript received February 8, 2012; revised September 5, 2012; accepted September 6, 2012. Date of publication September 18, 2012; date of current version January 24, 2013. The associate editor coordinating the review of this manuscript and approving it for publication was Prof. Wai-Kuen Cham.

C. Wang, Y. Yue, F. Dong, X. Ma, and G. Clapworthy are with the Department of Computer Science and Technology, University of Bedfordshire, Luton LU13JU, U.K. (e-mail: w-c05@mails.tsinghua.edu.cn; yong.yue@beds.ac.uk; feng.dong@beds.ac.uk; xiangyin.ma@beds.ac.uk; gordon.clapworthy@beds.ac.uk).

Y. Tao and H. Lin are with the State Key Laboratory of CAD and CG, Zhejiang University, Hangzhou 310058, China (e-mail: taoyubo@cad.zju.edu.cn; lin@cad.zju.edu.cn).

X. Ye is with the School of Computer Science, University of Lincoln, Lincoln LN6 7TS, U.K. (e-mail: xye@lincoln.ac.uk).

Color versions of one or more of the figures in this paper are available online at http://ieeexplore.ieee.org.

Digital Object Identifier 10.1109/TIP.2012.2219548

restore LSEDs. However, they only work well only for images with simple textures and often fail to handle highly textured images. This is because highly textured images can exhibit a wide spread of edges, beyond the capability of edge prediction.

The non-edge specific scheme, on the other hand, is not designed to carry out deblurring based on the detection or prediction of LSEDs, so it avoids the limitations of the edge specific scheme. There are two main approaches.

1) Adopting image measurements to favor sharp explanations [24]. As will be demonstrated in this paper, such measurements work only for a very small number of natural images. We will further demonstrate that finding a measurement robust to millions of natural images is almost impossible.
2) Marginalizing the sparse prior distribution [9], [25]. Levin et al. [16] proved that this approach leads to the true solution under the condition that the image size is much larger than the kernel size. Although it has a sound theoretical foundation, we find that its performance is very unstable, mainly due to the variation of the sparse priors over different images. For example, a sparse prior distribution learned from highly structured images [9] may work very poorly on simply structured images.

In short, the performance of the edge-specific scheme is greatly limited by its inability to recover a wide variety of image edges. On the other hand, the non-edge specific scheme suffers from the statistical variations to be found in natural images. This leads to poor robustness towards image diversity.

To address these problems, this paper proposes a novel non-edge specific adaptive scheme (NEAS) for blind motion deblurring. While NEAS belongs to the non-edge specific scheme, it is designed to deal with statistical variations of images and increases the robustness by adopting an adaptive approach. Consequently, NEAS overcomes the sensitivity to the variation of image edges or to the statistical variation of natural images associated with other methods.

NEAS is implemented through a novel prior that combines LSED prediction and prior distribution marginalization. The former provides an adaptive term to guarantee the robustness to statistical variation of natural images, while the latter offers a good initial value and a regularization term to guarantee the robustness to diverse image edges.

NEAS works very well on a very wide variety of images. Our experiments have shown that it outperforms existing methods on the standard dataset of Levin et al. and a huge image set built based on 1.2 million natural images in ImageNet. Notably, this superior performance was observed consistently on many different categories of natural images during our experiments.

In summary, the contributions of this paper are as follows.

1) It reveals that the robustness to natural image diversity is a significant problem for blind motion deblurring through in-depth analysis and experiments (Sections III and VI).
2) It identifies the source of sensitivity to natural image diversity in the existing methods and hence explains the cause of this poor robustness (Section III).
3) Based on this analysis, it proposes a novel adaptive scheme (i.e. NEAS) and demonstrates that it outperforms the state of the art by performing experiment on a huge set of natural images exhibiting wide diversity (Section IV and V).

The remainder of the paper is organized as follows. Section II describes related work, and Section III describes the problems associated with existing methods. NEAS is described in Sections IV and V, while Section VI presents the experimental results. Section VII discusses the limitations of NEAS, and Section VIII draws the final conclusions.

II. Related Work

Blind motion deblurring is an interesting subject to the image processing community, but many existing methods suffer from poor robustness towards the wide diversity to be found in natural images. Often, these methods have been subjected to relatively light testing in which the evaluation considers only experimental images or involves images numbering only in the dozens. We argue that a truly robust method should undergo rigorous evaluation using a much more extensive set of images which reflects the full diversity of form and content to be found in natural images. However, this robustness issue has not yet received much attention from the research community.

This section provides a brief review of the blind motion deblurring techniques related to NEAS. For a more comprehensive literature survey in this area, see [6], [7]. By convention, the blurring process is modeled as:

$$y = k \otimes x + n \tag{1}$$

where y is the observed blurred image, k is the blur kernel, x is the latent sharp image, n is the image noise, and $\otimes$ denotes the convolution operator.

Traditional methods cast blind motion deblurring into the maximum-a-posteriori (MAP) framework, which seeks a pair (x^*, k^*) that maximizes the likelihood $p(x, k|y) \propto p(y|x, k)p(x)p(k)$, in which the likelihood term $p(y|x, k)$ is the data fitting term, and $p(x)$ and $p(k)$ are the priors of the image x and kernel k, respectively. More specifically, this can be expressed as follows:

$$(x^*, k^*) = \arg\min_{(x,k)} \left\{ \frac{1}{2\sigma_n^2} ||k \otimes x - y||^2 + \rho(x) + \rho(k) \right\} \tag{2}$$

where σ_n is the standard deviation of noise n. Equation (2) holds for Gaussian noise. The first term is the data fitting term from (1), the second term $\rho(x) = -\log p(x)$ and the third term $\rho(k) = -\log p(k)$ are the energies of image x and kernel k respectively.

$\rho(x)$ can be expressed in terms of either Hyper-Laplacian [26], [27], Mixture of Gaussians [9] or using more complex forms to characterize high-dimensional properties [28], [29]. For natural images, $\rho(x)$ is sparse, i.e. the distribution of the gradients in natural images is sharply peaked at zero and relatively heavy-tailed, which is heavily deviated from standard Gaussian distributions. $\rho(k)$ can be either a uniform prior to cover Gaussian kernels according to [16] or a more sparse prior to model trajectory-like kernels according to [9], [20].

Equation (2) is generally solved by an iterative optimization that alternates between refinement of the blur kernel k and restoration of the image x until the convergence is reached.

It has been pointed out by [9], [16] that the solution for (2) is a blurred image rather than a sharp one, no matter whether $\rho(k)$ is uniform [16] or sparse [9]. This is because a sparse image prior favors blurred images, which means that a blurred image has lower energy than its sharp version. In fact, the global optimum solution of (2) is actually a blurred image, and the sharp version corresponds only to a local optimum. This increases the difficulty in obtaining the sharp image through optimization. We refer to this as MAP failure in this paper.

A. Edge Specific Scheme

To remedy the MAP failure, the edge specific scheme relies on the detection and prediction of large-scale step edges (LSED).

LSED detection-based methods [13], [15], [20] assume that sharp explanations are favored by (2) around step edges (i.e. sharp edges have lower energy than their blurred versions in (2)). However this assumption holds only for a few small windows around LSED.

The LSED prediction-based methods [11], [17], [18], [22] firstly restore sharp step edges and then use them to estimate a good initial kernel, which traps the optimization of (2) into the local minimum corresponding to the sharp solution.

The most commonly used approach to restore step edges is the shock filter: $x^{t+1} = x^t - sign(\Delta x^t)||\nabla x^t||dt$ with Δ, ∇ and dt denoting the Laplacian operator, gradient operator and the time step, respectively.

Since sharpening filters that includes the shock filter can only restore step edges, the LSED prediction-based methods cannot handle images in which the number of LSEDs is small, e.g. highly textured images. Xu et al. [18] use a gradient map to retain LSEDs by excluding narrow edges. However, their method is not robust as it fails to exclude a variety of types of edge to guarantee robust kernel estimation.

B. Nonedge Specific Scheme

The non-edge specific scheme does not rely on the recovery of one specific kind of edge. This consequently avoids the weakness exhibited by the edge specific scheme. One approach is to seek an image measurement that favors sharp explanations [24] (i.e. sharper images achieve lower measurement scores). But it is extremely hard for a measurement to work well for thousands of natural images, let alone for millions of examples.

A more robust solution [9], [25] is the marginalization method, which solves k by maximizing $p(k|y)$. This can be achieved through marginalizing the sparse distribution of x:

$$\begin{aligned} k^* &= \arg\max_k p(k|y) = \arg\max_k \int p(x, k|y)dx \\ &= \arg\max_k \int p(y|x, k)p(x)p(k)dx. \end{aligned} \tag{3}$$

It is been proved in [16] that (3) leads to the true solution under the condition that the size of x is much larger than the size of k according to Bayesian estimation theory. However, this is based on the assumption that the prior $p(x)$ is the same for all natural images. In fact, the deviation of $p(x)$ among natural images leads to significant performance variation of the marginalization method over different natural images.

C. Novelty

The NEAS proposed in this paper is an elegant combination of the marginalization method and the LSED prediction method. NEAS inherits the advantages of the non-edge specific scheme since it does not rely on the recovery of specific image edges. Meanwhile, NEAS adopts a novel adaptive prior, leading to the capability of handling the variation of sparse image priors that exists in natural images in an adaptive manner. Consequently, NEAS achieves a high degree of robustness and a good performance across a wide variety of natural images.

Notably, this paper focuses entirely on the issue of algorithm robustness to image diversity. Other issues such as blur formulation and optimization are not at the center of this research. And only spatially uniform blurs are considered in this paper. Space-variant blur models can be found in [21], [23], [30], [31].

III. Analysis

This section analyzes the fundamental causes of poor robustness of the existing blind motion deblurring techniques. We will identify the source of their sensitivity to the diversity of natural images.

The analysis is based on experiments carried out on a huge image set, ImageNet [19], which offers a comprehensive coverage of natural images from the real world. It features 12 subtrees, containing a total of 1.2 million high quality images spread over 5247 categories.

We use the Kullback–Leibler (KL) distance to quantify the difference of derivative distributions between natural images. Since a sparse image prior concerns the distribution of derivatives, KL distance is an important measure to assess the priors. Based on the KL distance, we quantize all the images from ImageNet into 20 category bins according to their KL distances to the model image in Fig. 1(a); the centroid image of each bin is shown in Fig. 2. Analysis has been performed on the images under this categorization.

The experiments needed to artificially blur all of the 1.2 million images from ImageNet using different blur kernels, creating pairs of blurred and sharp images. Generating blurred images using artificial kernels is a common practice in much blind motion deblurring research [16]. Since the true motion blur kernel is unknown, different artificial kernels are often used to mimic the real motion blur. Our analysis involved

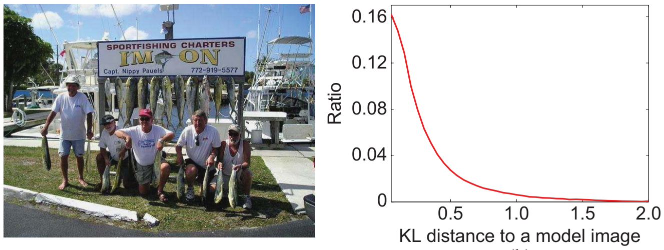

(a) (b)

Fig. 1. (a) Model image of complex textures. (b) Distribution of the KL distance between the derivative distribution of each image in ImageNet and that of the model image in (a). We quantify the KL distance in 20 bins.

the use of different blur kernels, including those illustrated in Fig. 9(b) and Fig. 5(b).

Briefly, four key findings are revealed by the analysis. The first confirms an observation by Levin et al. [16], but with much more extensive testing; the other three are original. The remainder of this section will provide detailed analysis towards these findings, followed by an illustration of their impact on the robustness of existing methods.

Key Findings 1 and 2 target the edge specific scheme, including LSED detection [13], [15], [20] or prediction [11], [17], [18], [22].

A. Key Finding 1

A sparse prior favors sharp explanations only in a few small windows of natural images.

This finding implies the MAP failure, i.e. a sparse prior does not favor the sharp version of the blurred image. To illustrate this on millions of images, we conducted two experiments.

Our first experiment is designed to compare the energy between the artificially blurred and sharp image pairs using a sparse prior. The blur kernel is shown in Fig. 9(b). For the sparse image prior, we employ the Hyper-Laplacian prior as in [16]: $\rho(x) = \sum_{\gamma,j} \|f_{\gamma,j}(x)\|^{\alpha}$ where $f_{\gamma,j}(x)$ denotes the output of $f_\gamma \otimes x$ at pixel j. f_γ has two components in horizontal and vertical directions, i.e. $f_\gamma = \{f_h, f_v\} = \{[1, -1], [1, -1]^T\}$, and $\alpha = 0.6$.

Among the 1.2 million images, we find that only 317 sharp images have lower energy than the corresponding blurred images, accounting for only 0.0264% of the total. All of these 317 images are composed mainly of step edges, as shown in Fig. 3.

In the second experiment, we assess the sparse prior $\rho(x)$ within differently sized local windows in a natural image and observe how many of them favor the sharp version. Fig. 4(a) shows the average percentage of the windows sized at 25×25 that favor the sharp versions within the 20 category bins. It shows that this percentage is quite small for highly textured images ($< 0.15\%$). Further, the blurred versions are favored almost at all windows ($> 99.99\%$) if 45×45 windows are used in the experiment.

LSED detection-based methods [13], [15], [20] in the edge specific scheme assume that sharp explanations are favored by (2) around LSEDs. However, both of the experiments above show that this assumption holds only for a few small windows of natural images. This finding leads to the conclusion that LSED detection-based methods are far from being robust to natural images.

B. Key Finding 2

The number of LSEDs available within a natural image is usually insufficient for a robust kernel estimation.

This finding is broken down into 2 sub questions.

1) How many edges are required for accurate kernel estimation?
2) How many LSEDs can be recovered from a natural image?

To answer the first question, our experiment estimates the kernels from the artificially blurred images (Fig. 5(b) shows the true kernel). Then both of the estimated and true kernels are used to recover the sharp image version, allowing for the assessment of the quality of the estimated kernels.

More specifically, we randomly select 100 blurred and sharp pairs from each bin of the entire image set and estimate their kernels using large gradient values in a least square manner as in [17]. Based on the estimated kernel, the sharp images are recovered using the fast sparse deconvolution method [27] with the default parameters. To assess the accuracy of the estimated kernels, we follow Levin et al. [16] by using the sum of squared differences (SSD) ratio between the deconvolution error with the estimated kernel and the deconvolution error with the true kernel.

Figure 5(a) shows the SSD ratio against the ratio between the number of gradient values and the kernel size. Empirically, SSD ratios below 3 are regarded as visually acceptable [16]. The figure shows that the number of gradients needs to double the kernel size in order to reach a satisfactory estimation (SSD<=3). Figure 5(b) shows two results with different numbers of gradient values, in which the right image (SSD = 852, recovered by using gradients that double the kernel size) contains less ringing artifacts than the left (SSD = 1247, recovered by using gradients sized equivalently to the kernel).

The answer to the second sub-question is divided into 2 cases, depending upon whether the LSEDs are isolated [22] or not [17], [18].

1) The number of isolated LSEDs is low in natural images. Figure 6(a) shows the average numbers of LSEDs detected by [22]. This is particularly true for highly textured images, with many such examples having fewer than 500 isolated LSEDs. One example is shown in Fig. 6(b).
2) For non-isolated LSEDs, generally we are able to recover only one specific type of LSED, i.e., the LSEDs with a size larger than the blur kernel [18], using sharpening filters out of the 7 types of edges of natural images classified by [32], as shown in Fig. 7.

The blur kernel used in this experiment is shown in Fig. 9(b) (sized 45×45). The step edges are computed by $(1/L)\sqrt{\sum_l \cos(2\theta_l)^2 + \sum_l \sin(2\theta_l)^2}$, following the work of [33]. $\theta_l \in [0, \pi]$ denotes the orientation of the edge, and L denotes the number of the edges. Only edges with a large

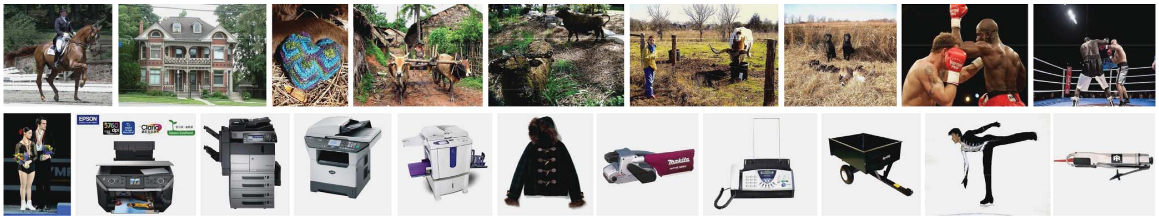

Fig. 2. Centroid images of 20 quantized category bins in Fig. 1(b). The KL distances increase from top to bottom and left to right.

Fig. 3. Examples for which sharp images are favored by the sparse derivative prior. These images are mainly composed of step edges.

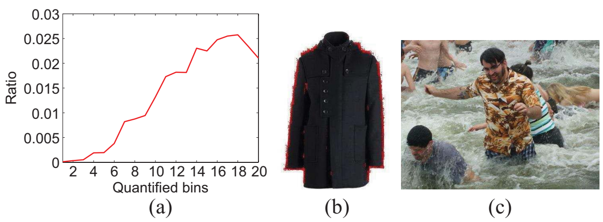

Fig. 4. (a) Average ratio of windows in which the sharp explanation is favored. (b) Simply textured example containing many windows (marked in red) in which the sharp explanation is favored by the sparse prior. (c) Complex textured example containing few windows in which the sharp explanation is favored by the sparse prior.

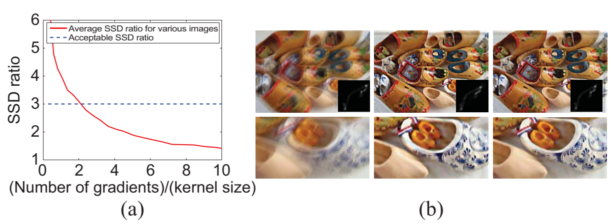

Fig. 5. (a) SSD ratios as a function of the number of gradient values adopted for kernel estimation. (b) Testing blurred example together with a kernel, the result (SSD = 1247) estimated using r^2 gradient values, and the result (SSD = 852) estimated using $2r^2$ gradient values, with r denoting the width of the blur kernel. The close-up views reveal the quality of the estimated kernels.

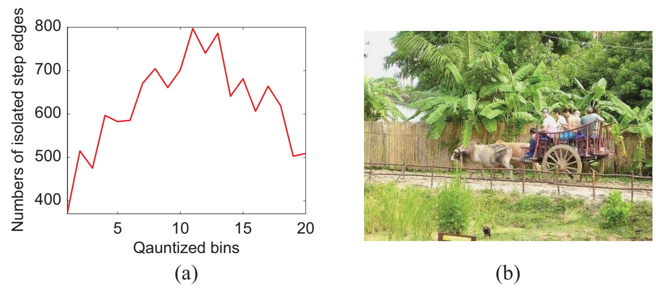

Fig. 6. (a) Average numbers of the detected isolated LSED using the method in [22], for the 20 quantized category bins. (b) Highly textured example, which contains no isolated LSED for [22].

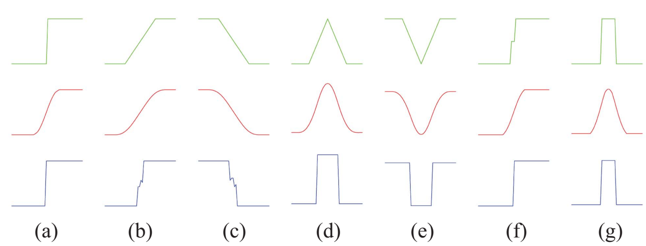

Fig. 7. (a)–(g) sharp edges, the blurred edges, and the sharpened edges by the shock filter for seven kinds of natural edges. From (a) to (g) are step, concave slope, convex slope, roof, valley, staircase, and peak edges. Only the step edge is accurately recovered. Notice that the height of the peak edge becomes smaller after being sharpened.

metric (i.e. greater than 0.5) are retained. Finally, we exclude narrow edges to obtain LSEDs using the gradient map [18] $g_m(y_i) = \|\sum_{\gamma,j\in\Omega(i)} f_{\gamma,j}(y)\|/(\sum_{\gamma,j\in\Omega(i)} \|f_{\gamma,j}(y)\| + 0.5)$ where $\Omega(i)$ denotes the neighborhood window of pixel i, and $f_{\gamma,j}(y)$ denotes the output of $f_\gamma \otimes y$ at pixel j. This process uses a threshold of 0.5 for g_m.

Fig. 8(a) shows the average number of detected LSEDs in the 20 category bins. One such example is given in Fig. 8(b), which shows that the method works sufficiently well.

By putting the answers to these two sub-questions together, we can see that natural images, especially those that are highly textured, often do not have sufficient LSEDs to support a satisfactory recovery of blur kernels at normal sizes (e.g., 45×45).

The LSED prediction-based methods in the edge specific scheme attempt to restore sharp step edges by using the inverse Radon Transform [22] or deterministic sharpening filters [17], [18] before applying the restored sharp edges for kernel estimation.

For the Radon Transform approach [22], the LSEDs should be isolated. Our statistics have shown that a normal sized kernel (e.g. 45×45) cannot be accurately estimated due to the lack of LSEDs in many natural images.

For the approach by [17], [18] adopting the sharpening filter, non-isolated LSEDs are allowed. However, as shown above, the types and sizes of recoverable edges are very limited.

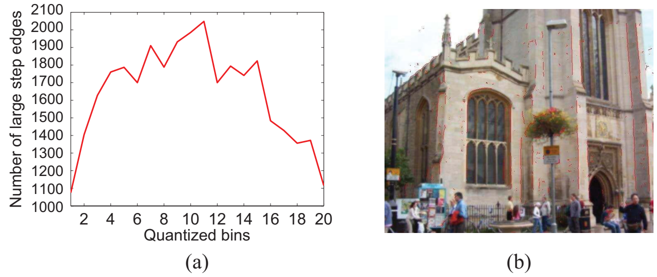

Fig. 8. (a) Average numbers of the detected LSED for the 20 quantized category bins, using our detection method. (b) Example to show the accuracy of our detection method. The LSED are marked in red.

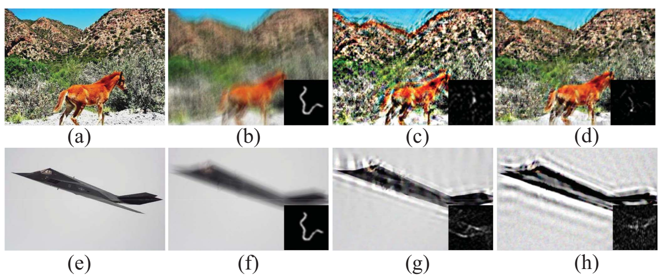

Fig. 9. Two failure examples for the LSED prediction methods [17], [18]. The top images demonstrate that complex textured images might have insufficient large step edges. The bottom examples show that extremely simple images cannot provide sufficient edges. (a) and (e) Sharp images. (b) and (f) Blurred images together with the blur kernel. (c) and (g) Results by Cho *et al.* [17]. (d) and (h) Results by Xu *et al.* [18].

Including other types of edges in kernel estimation might totally damage the result [18].

We have tested the LSED-prediction based methods on highly textured images in the first three category bins of ImageNet using the method of [17] and found that the failure (SSD$>$3, an example illustrated in Fig. 9(c)) is associated with 17.45% of the total. It has also been observed that the number of LSEDs in an extremely simple image is also small (i.e. only hundreds of non-zero gradients) hence is insufficient to recover kernels at normal sizes.

Key Finding 2 suggests that LSED-prediction based methods are not able to handle a considerable proportion of the images in ImageNet, so they are deemed not to be robust.

By considering Key Findings 1 and 2 together, we draw the conclusion that the edge-specific scheme is sensitive to image diversity due to an insufficient number of recoverable LSEDs.

Xu et al. [18] have proposed a gradient map to exclude narrow edges in order to retain only step edges. However, their method cannot exclude unwanted edges in order to guarantee robustness, as shown in Fig. 9(d).

Key Finding 3 and 4 target the non-edge specific scheme, which resorts to image measurement [24] or marginalization of image distribution [9], [25] to favor sharp explanations.

C. Key Finding 3

Finding a robust measurement that favors sharp explanations for diverse natural images is nearly impossible.

Krishnan et al. [24] found a normalized sparsity measurement of gradients l_1/l_2 (this is not a prior

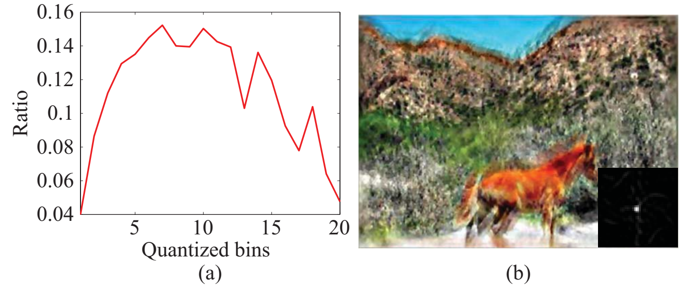

Fig. 10. (a) Ratios of the 1.2 million images for which l_1/l_2 works, for each bin. (b) Result from the method using l_1/l_2 [24] for the blurred image shown in Fig. 9(b).

because $\int exp(-l_1/l_2) = \infty)$ that favors sharp images. l_p denotes the p-norm on the gradients and $l_1/l_2 = \sum_{\gamma,j} \|f_{\gamma,j}(x)\| / \sqrt{\sum_{\gamma,j} \|f_{\gamma,j}(x)\|^2}$. This measurement works well for Levin et al.'s 32 image dataset [16].

However, our work has found out that this measurement works poorly on images within ImageNet. By comparing the blurred (via kernel Fig. 9(b)) and sharp image pairs in l_1/l_2, we find that the sharp version is favored in 110,107 images, accounting for only 9.18% of the total. Figure 10(a) gives the percentage of the images in which l_1/l_2 works well in each bin. It is clear that l_1/l_2 is apt to fail for highly textured images. Figure 10(b) shows the result of a failure.

One question thus arises: is there a robust measurement consistently favoring sharp images? In fact, this question can be seen as a dimensionality reduction and classification problem. Finding such a measurement is equivalent to projecting the image vector down to a single dimension while maximizing the separation of the sharp images from their blurred versions. This problem is known as Fisher's discriminant in Machine Learning. The projection to one dimension leads to considerable loss of information. The classes that are well separated in the original high-dimensional space might become strongly overlapping. Finding such a robust measurement for extremely diverse natural images is nearly impossible.

To illustrate this, we use the blur kernel in Fig. 9(b) at various sizes, including 5×5, 9×9, 13×13, 17×17, 21×21 together with noise of a standard deviation of 0.01 to synthesize the blurred versions artificially. 10,000 sharp images in ImageNet with their blurred versions are used as the training set, and both the linear and non-linear projections are tested.

For linear projection, we adopted Fisher's linear discriminant [34] to solve for the measurement, and found that only 61.2% of the images could be correctly classified. Hence, a linear robust measurement does not exist. For nonlinear projection, we adopted the kernel Fisher discriminant [34]. Among the kernel functions [34], the radial basis function produced the best results: 64.7% of all the images could be correctly classified. This reveals that it is nearly impossible for image measurements to remedy the MAP failure.

These experimental results support Key Finding 3.

D. Key Finding 4

Sparse gradient priors vary greatly among natural images.

To illustrate the diversity among natural images, we measure the KL distances between the derivative distribution of the images in ImageNet and that of a model image shown in Fig. 1(a). This results in a heavy-tailed distribution, whose kurtosis measurement equals 6.65, as shown in Fig. 1(b). We also find that the KL distance increases when the image texture becomes simpler. For simple man-made scenes which consist of only a few step edges, the KL distances are quite large, as demonstrated by the centroid images in Fig. 2. All these observations demonstrate a broad diversity of derivative distributions among the images.

The marginalization methods learn a sparse distribution prior from a single highly textured model image [9], [25]. However, applying the prior learned from a single image to highly diverse natural images leads to significant variation of performance over different natural images.

To illustrate this, we carried out an experiment by applying the estimated kernels to artificially blurred images and subsequently comparing the SSD errors using the true sharp images. The images involved included 100 randomly selected blurred and sharp image pairs from all the category bins of ImageNet. We used the blur kernel in Fig. 9(b), together with Gaussian noise at a standard deviation of 0.01. The marginalization method from [25] was used to solve for the kernels. The sparse non-blind deconvolution method in [26] with its default parameters was used to deblur the images.

Figure 11(a) shows the average SSD errors. Since the sparse image prior is often trained from a highly structured image [9], [25], it works poorly for other types of image. Figure 11(b) provides a failure example owing to the significant differences in priors.

Key Finding 3 and 4 suggest that the non-edge specific scheme is sensitive to image diversity in natural images.

The theoretical and experimental analysis above demonstrates that the difficulties in image edge recovery lie in the diversity of image edges and the prediction of only specific edges leads to poor robustness in deblurring. Furthermore, due to the diversity of natural images, the sparse priors learned from certain images may not be applicable to others.

IV. Proposed Method: NEAS

We address the problems mentioned above by proposing a non-edge specific adaptive scheme (NEAS). NEAS is based on the marginalization method [25], which is non-edge specific, and employs a prior that is adaptive to individual images. Our experiments have shown that this novel prior is able to improve the robustness of blind motion deblurring significantly - see Section VI.

This section firstly proves that an adaptive prior in its theoretical form should lead to the true solution of deblurring. Then we show how to formulate the adaptive prior and how to apply it to the energy function in an iterative and multiscale manner to allow for a traceable solution.

A. Adaptive Prior and True Solution

Ideally, an adaptive prior would be a Gaussian centered around the true sharp image x^*: $\frac{1}{\sqrt{2\pi}\sigma_R} exp(-\frac{1}{2\sigma_R^2}\|x - x^*\|^2)$.

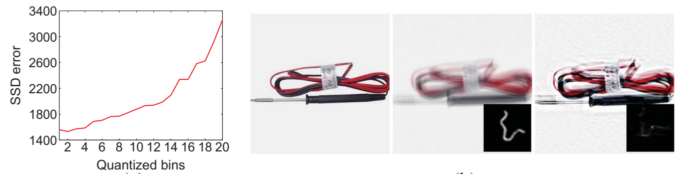

(a) (b)

Fig. 11. (a) Average SSD errors of the results by the marginalization method [25], for all the 20 quantized category bins. (b) Sharp version, blurred version, and the deblurred version of a failure example for the marginalization method [25] due to large prior variance.

This prior is adaptive since it is regularized by each image x^*. By using this prior, the marginalization method produces the true solution. This can be proved as follows.

If we integrate x using (3), we can express $p(y|k)$ analytically and obtain a Gaussian

$$Y \sim \frac{1}{\sqrt{2\pi}\sigma_Y} exp(-\frac{1}{2\sigma_Y^2}\|Y - KX^*\|^2) \quad (4)$$

where Y, X^*, K denote the Fourier transforms of y, x^* and k respectively, and $\sigma_Y^2 = \sigma_R^2\|K\|^2 + \sigma_n^2$. By assuming a uniform prior on k as [25], we have $\arg\max_k p(k|y) = \arg\max_k p(y|k)$. So maximizing (4) is equivalent to maximizing (3). Since (4) is maximized when $KX^* = Y$, the marginalization method produces the true solution $K = Y/X^*$.

However, we cannot use the Gaussian prior $\frac{1}{\sqrt{2\pi}\sigma_R} exp(-\frac{1}{2\sigma_R^2}\|x - x^*\|^2)$ to obtain the true kernel as practically we do not know the final target x^*.

B. Two-Component Prior for the Marginalization Method

To overcome the problem, we adopt a two-component sparse prior $p(x)$:

$$p(x) = p_S(x)p_R(x) \quad (5)$$

where $p_S(x)$ is the sparse derivative prior, and $p_R(x)$ is the adaptive prior.

The adaptive prior $p_R(x)$ uses the result x_l from LSED prediction-based methods [17] to approximate the true sharp image x^*. It is assumed to be in Gaussian form centered on the predicted LSEDs in the gradient domain: $p_R(x) = \frac{1}{\sqrt{2\pi}\sigma_R} exp(-(1)(2\sigma_R^2)\sum_\gamma \|f_\gamma(x) - M \circ f_\gamma(x_l)\|^2)$ where M denotes the mask of LSED and $\circ$ represents the element-wise multiplication operator. The LSEDs (i.e. mask M) are identified using the method presented under Key Finding 2 in Section III.

$p_S(x)$ is added to stop the constraints from disappearing. $p_R(x)$ disappears in highly structured images, in which there are few LSEDs (i.e. M becomes 0). As mentioned earlier, the existing marginalization methods [9], [25] apply a single sparse distribution $p_S(x)$ to all images, which is not robust. By using the novel adaptive prior in (5), the results are pulled towards individual images by the prior $p_R(x)$. Then our new marginalization method solves for k by $\arg\max_k \int p(y|x,k)p_R(x)p_S(x)p(k)dx$.

C. Two-Component Prior for LSED Prediction-Based Method

An inherent problem in (5) is that x_l might be inaccurate because LSED prediction-based methods are edge specific, which violates the motivation of NEAS. This is particularly true for highly structured images. The limitations of LSED prediction-based methods compromise the advantages of the adaptive prior. To obtain an accurate x_l, we integrate the adaptive prior of (5) into the LSED prediction-based methods while assuming $p_R(x)$ to be a Gaussian centered on x_m which is the result of the marginalization method. Then the energy function of the LSED prediction-based method becomes:

$$\frac{1}{2\sigma_n^2}\|k \otimes x - y\|^2 + \frac{1}{2\sigma_R^2} \times \sum_{\gamma} \|f_\gamma(x) - M \circ f_\gamma(x_m)\|^2 + \rho(x) + \rho(k). \quad (6)$$

Obviously, $p_R(x)$ acts as a regularization term to pull the result of (6) towards x_m in order to produce an accurate result x_l.

D. Iteration:

In a nutshell, NEAS works as an iterative process that alternates between the marginalization method and the LSED prediction-based method. The former provides a good initial value and a regularization term for the latter. The latter provides an adaptive prior for the former. In this manner, the marginalization method and the LSED prediction based method are regularized by each other. The adaptive prior in (5) provides a simple way to combine these two leading methods in the framework of NEAS. Figure 12 demonstrates the impact of the adaptive prior.

The enhanced robustness in NEAS can be explained from the perspective of energy minimization.

Essentially, the marginalization method provides a better initial value and an energy constraint which allow the LSED prediction-based method to adaptively cope with image diversity. It is known from [16] that a sharp solution corresponds to a local minimum instead of a global minimum of the energy function in (2). Hence, we aim to converge at the desired local minimum instead of at the global minimum.

To achieve this, we need to place the initial value within a small neighborhood of the local minimum for the true sharp solution and hence allow the local-minimum based method to converge at the desired position. NEAS adopts the result of the marginalization method as the initial value.

The initial values of the traditional LSED prediction-based methods are obtained from the shock filters [17], [18]. They are edge sensitive and can be very far from the true solution. This is particularly true for images with complex textures. As shown in Fig. 13, the better initial value from the marginalization methods improves the result significantly.

Also, through the designed iteration, the results of the marginalization are used as a constraint to prevent the LSED prediction-based method from drifting away from the true solution in (6). Such a drift occurs very frequently in LSED prediction-based methods due to inaccurately recovered narrow edges [18]. The new constraint allows the sharp solution to remain as a good local minimum. Figure 13(g) demonstrates the impact of the energy constraint.

(a) (b) (c) (d)

Fig. 12. (a) and (b) Results by the marginalization method, not using and using our adaptive prior, respectively, for the blurred image in Fig. 11(b). (c) and (d) Results by the marginalization method, not using and using our adaptive prior, respectively, for the blurred image in Fig. 9(b).

Algorithm 1 shows the basic iteration process of NEAS.

E. Multiscale Scheme

In practice, we adopt a multi-scale approach to refine both k and x from coarse to fine. At each scale, we perform the iteration process illustrated in Algorithm 1.

The purpose of following the multiscale scheme is to ensure satisfactory results from the marginalization method. In fact, performing the marginalization method at the full image scale sometimes fails to provide a good initial value and energy constraint owing to the image diversity. But we have observed that the marginalization method can achieve extremely good results at coarse scales even if the estimated kernel at the full scale is inaccurate. This is because the down-sampling smoothes out the error in the kernel estimation, leading to a smaller deconvolution error at the coarse scales.

To illustrate this, we take Fig. 13(b) as an example. Figure 13(h) shows the SSD error at each scale. At the coarsest layer, the result is nearly identical to the true solution (per-pixel SSD error$<$0.001) and the SSD gap grows with the increase of image resolution.

The joint prior (5) improves the robustness of the marginalization method from coarse to fine, producing a much better result, as shown in Fig. 13(g, h). This demonstrates that NEAS can handle challenging examples beyond the capabilities of both the marginalization and the LSED prediction based methods.

V. Implementation Details

Here we give the details of our implementation of the marginalization and LSED prediction based method in NEAS.

A. Marginalization Method

In the marginalization method, we assume the prior in (5) on x, a uniform prior on k and a Gaussian prior on image noise n, obtaining

$$\begin{aligned} p(x,k|y) &\propto p(y|x,k)p_S(x)p_R(x) \\ &\propto p_S(x)exp(-\frac{1}{2\sigma_n^2}(y - k \otimes x)^2) \\ &\quad \times exp(-\frac{1}{2\sigma_R^2}\sum_{\gamma}(f_\gamma(x) - M \circ f_\gamma(x_l))^2). \quad (7) \end{aligned}$$

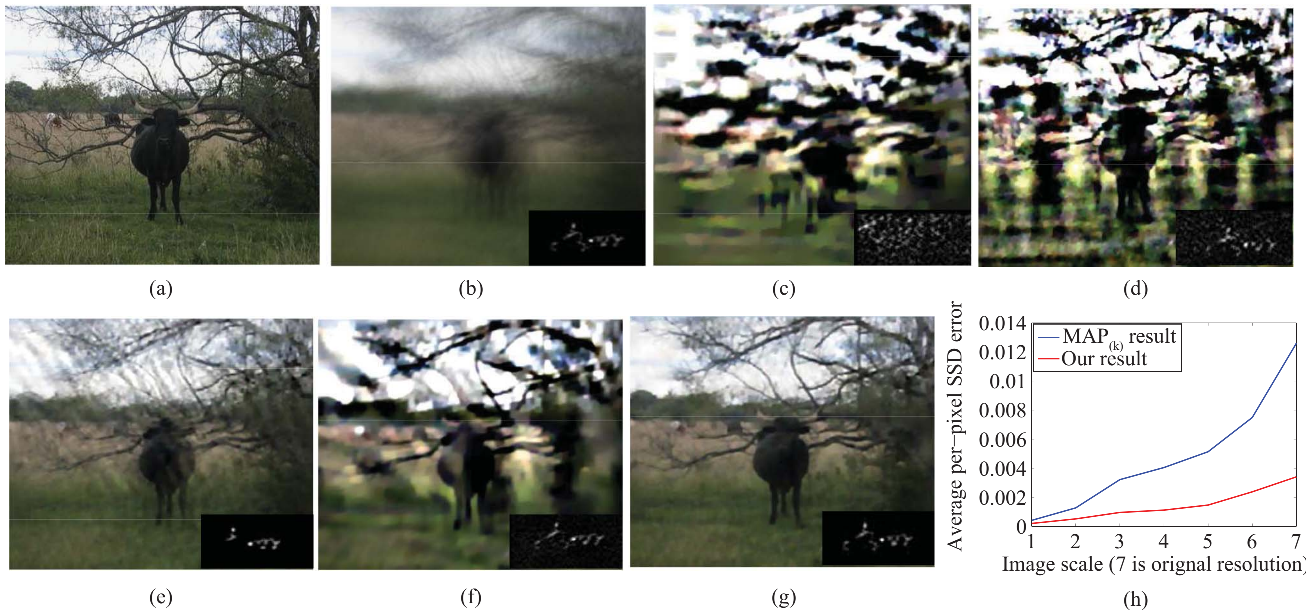

Fig. 13. Impact of a good initial value and our energy constraint. (a) Sharp image. (b) Blurred image with the blur kernel. (c) Result from the LSED prediction-based method [17]. (d) Result from the LSED prediction-based method [18]. References [17] and [18] initialize the value using a sharpening filter. (e) Result from the marginalization method [25]. (f) Result from LSED prediction-based method with the image in (e) as an initial value. Note that the kernel has a similar shape to that of the true kernel, but contains too much noise which cannot be removed using a simple threshold method. (g) Result from our NEAS, which takes the image in (d) as an initial value together with our energy constraint. (h) Average per-pixel SSD errors at each scale for the results from the marginalization method (blue line) and our NEAS (red line).

Due to the non-convex sparse prior $p_S(x)$, there is no closed-form solution to $\arg\max_k \int p(x,k|y)dx$. We adopt Levin et al.'s EM optimization [25] to solve for k.

In the E-step, a Gaussian distribution $q(x)$ is built using the variational free energy strategy to approximate $p(x|y,k)$ to solve for the mean image and the covariance. The M-step solves for the best kernel given the mean image and the covariance. Since every step improves log $p(y|k)$ [25], this algorithm produces very satisfactory results. For the sparse prior $p_S(x)$, Levin et al. [25] adopt a mixture of J Gaussians $\sum_{j=1}^{J} \frac{\pi_j}{\sqrt{2\pi}\sigma_j} exp(-\frac{1}{2\sigma_j^2}\sum_\gamma \|f_\gamma(x)\|^2)$ with π_j denoting the weight for the j^{th} component. For more details about the EM algorithm, refer to [25].

Our work is built on the implementation of [25]. The main modification lies at the integration of the novel adaptive prior in (5). Algorithm 1 gives the detailed steps and mathematical equations.

B. LSED Prediction-Based Method

In the LSED prediction-based method, the large step edges are firstly sharpened by the shock filter as in [17], and then the energy function:

$$\frac{1}{2\sigma_n^2}\|k \otimes x - y\|^2 + \frac{1}{2\sigma_R^2}\sum_\gamma \|f_\gamma(x) - M \circ f_\gamma(x_m)\|^2 + \sum_\gamma \|f_\gamma(x)\|^\alpha + \|k\|^\alpha \quad (8)$$

is optimized by iteratively updating x and k. Note the last two terms are the Hyper-Laplacian priors of the image and kernel, respectively. With fixed k, Equation (8) can be simplified to:

$$\frac{1}{2\sigma_n^2}\|k \otimes x - y\|^2 + \frac{1}{2\sigma_R^2}\sum_\gamma \|f_\gamma(x) - M \circ f_\gamma(x_m)\|^2 + \sum_\gamma \|f_\gamma(x)\|^\alpha \quad (9)$$

which can be efficiently optimized using a lookup table [27].

By fixing x, Equation (8) is written as $\frac{1}{2\sigma_n^2}\|k\otimes x-y\|^2+\|k\|^\alpha$ which can be easily solved by using the IRLS method [26].

VI. Experiments

We compare NEAS with five leading methods - Fergus et al. [9], Levin et al. [25], Krishnan et al. [24], Cho et al. [17] and Xu et al. [18]. The first two of these are marginalization methods, while [24] is based on the measure l_1/l_2. All three methods belong to the non-edge specific scheme. The other two methods [17], [18] are LSED prediction-based methods, which belong to the edge specific scheme.

The proper way to compare the robustness of blind motion deblurring methods to image diversity is to perform them on a huge dataset containing millions of images. However, many leading approaches are computationally prohibitive at such a large scale. As a reference, it would take about 22 years on a 2.66 GHz Intel Xeon CPU to deblur 1 million images with a small kernel of 35×35 pixels, using the efficient marginalization method of Levin et al. [25], while the marginalization method from Fergus et al. [9] is even 10 times slower.

To make the experiment feasible, we randomly select 20 images from each of the category bins in Fig. 1 in order to cover the image diversity, thus obtaining 400 sharp images.

Algorithm 1 Implementation of NEAS

The marginalization method: iterating 1, 2 and 3 for five times

1. Update weights: $W_\gamma(i,i) = \sum_j (\omega_{i,\gamma,j}/\sigma_j^2)$ with

$$\omega_{i,\gamma,j_o} = \left(\frac{\pi_{j_o}}{\sigma_{j_o}} exp(\frac{-E(\|f_{i,\gamma}\|^2)}{2\sigma_{j_o}^2})\right) / \left(\sum_j \frac{\pi_j}{\sigma_j} exp\left(\frac{-E(\|f_{i,\gamma}(x)\|^2)}{2\sigma_j^2}\right)\right)$$

2. Update C and x_m: $C(i,i) = 1/A_x(i,i)$ and $A_x x_m = b_x$ with $A_x = \frac{1}{\sigma_n^2} T_k^T T_k + \sum_\gamma T_{f_\gamma}^T (W_\gamma + \frac{1}{\sigma_R^2}) T_{f_\gamma}$ and $b_x = \frac{1}{\sigma_n^2} T_k^T y + \frac{1}{\sigma_R^2} diag(V_M) \sum_\gamma (T_{f_\gamma}^T f_\gamma(x_l))$ where T_k, T_{f_γ} and V_M denotes the block Toeplitz matrixes of k, f_γ and M, and $diag()$ produces a diagonal matrix.
3. Update k: solve $min_k \frac{1}{2} k^T \overline{A}_k k - \overline{b}_k^T k \quad s.t. \quad k \geq 0$ with $\overline{A}_k(i_1, i_2) = \sum_i x_m(i+i_1) x_m(i+i_2) + C(i+i_1, i+i_2)$ and $\overline{b}_k(i_1) = \sum_i (x_m(i+i_1) y(i))$

   LSED prediction-based method: iterating 4, 5 and 6 for five times
4. Sharpen the LSED of x_m using the shock filter as in [17]: $x_m = x_m - sign(\Delta x_m) \sum_\gamma ||f_\gamma(x_m)|| dt$ with Δ denoting the Laplacian operator and $dt = 0.8$.
5. Update x_l: $min_x \frac{1}{2\sigma_n^2} \|k \otimes x - y\|^2 + \frac{1}{2\sigma_R^2} \sum_\gamma \|f_\gamma(x) - M \circ f_\gamma(x_m)\|^2 + \sum_\gamma \|f_\gamma(x)\|^\alpha$
6. Update k: $min_k \frac{1}{2\sigma_n^2} \|k \otimes x - y\|^2 + \|k\|^\alpha$

We blur each image using the four blur kernels shown in Fig. 14(c) with noise created at a standard deviation of 0.01. These kernels are selected from related work [18], [35] with sizes ranging from 25×25 to 45×45. Consequently, we obtain a large testing dataset which includes 1600 blurred images with ground truth. Deblurring this dataset still takes several months of computing time for most of the current leading methods [9], [24], [25].

Apart from using our large testing dataset, we have also tested these approaches on Levin et al.'s dataset which contains only 32 blurred images. Some methods produce good results on Levin et al.'s small dataset but work poorly on our large testing dataset. We have further tested these approaches on many challenging examples with large blur kernels that span up to 100 pixels in width or height.

In our experiments, the standard deviation σ_n of image noise is set to 0.01. We adaptively set the standard deviation of $p_R(x)$ as $\sigma_R = 10\sigma_n$. The Matlab implementation takes about 5 minutes to estimate a 35×35 kernel for a 300×300 image.

A. Results on Levin et al.'s Dataset

For fairness, we make a quantitative comparison between NEAS against the leading methods by looking into the experimental results from the published papers.

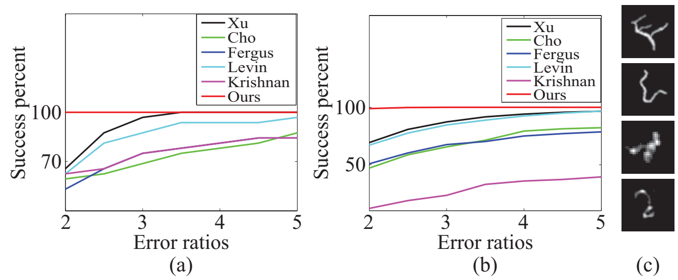

Fig. 14. Quantitative results by Xu *et al.* [18], Cho *et al.* [17], Fergus *et al.* [9], Levin *et al.* [25], Krishnan *et al.* [24], and our method. (a) Cumulative histogram of error ratios for Levin *et al.*'s dataset, including 32 images. (b) Cumulative histogram of error ratios for our large dataset, which includes 1600 images. (c) Ground truth kernels for our large dataset.

Following [16], [25], we measure the SSD ratio between the deconvolution results with the estimated and ground-truth kernels. Figure 14(a) plots the cumulative histogram of error ratios. Empirically, error ratios below 3 are visually plausible. All the methods produce good results with success rates over 60%. It shows that our SSD ratios are always below 2, which is better than those from the other approaches.

B. Results from Large Synthesized Dataset

Using the executable files or Matlab codes available online, we have tried to adjust the algorithm parameters to obtain the best quantitative results of [9], [17], [18], [24], [25] on our large testing dataset. Figure 14(b) plots the cumulative histogram of error ratios.

Xu et al.'s method slightly outperforms the method of Levin et al., while the methods of Cho et al. and Fergus et al. have similar performance. Although Krishnan et al.'s method produces nice results on Levin et al.'s small dataset, its performance on our large data set is very unreliable, which verifies the observation in Section III that l_1/l_2 is not a robust measure for blind motion deblurring. A large margin can be observed between our method and the others.

Figure 15 shows the results on four different images. Figures 15(a) and (b) are two images containing many large step edges. The methods of Cho et al. and Xu et al. produce nice results, but those of Fergus et al. and Levin et al. cannot estimate the trajectory shapes of the kernels since their priors are not robust.

Figure 15(c) and (d) are two images composed of various edges. The methods of Cho et al. and Xu et al. are unreliable as there are insufficient large step edges. The results by Fergus et al. and Levin et al. are much better, though they are still not quite accurate.

In comparison, the results of NEAS on these four diverse images are all very satisfactory. More results are included in the supplementary materials.

C. Examples With Large Blur Kernels

Figures 16(a) and (b) are two blurred images [18] mainly composed of step edges. The kernel sizes are 95×95 pixels and 55×105 pixels, respectively. The large blurs are beyond the capability of the methods of Fergus et al. and Levin et al.

Fig. 15. Comparison on four images in our large dataset. From top to bottom are the sharp images, the blurred images, the results by Xu *et al.* [18], Cho *et al.* [17], Fergus *et al.* [9], Levin *et al.* [25], Krishnan *et al.* [24], and by our method. (a) and (b) Two images containing many large step edges. (c) and (d) Two images, which lack step edges.

Although the methods of Krishnan et al. and Cho et al. can estimate the trajectory shapes of the kernels, the results have many artifacts, which demonstrates the inaccuracy of the kernel estimation. In contrast, both NEAS and Xu et al.'s method produce nice results.

Figures 16(c) and (d) are two highly textured images with few step edges. The kernel sizes are 65×65 pixels and 55×55 pixels, respectively. The methods of Cho et al., Xu et al. and Krishnan et al. are all unreliable. Though the results by Fergus et al. and Levin et al. are much better, they are still inaccurate. In comparison, the results from NEAS are very satisfactory. More examples can be found in the supplementary materials.

VII. Limitations

The experiments on the large dataset reveal a limitation of NEAS - it fails to handle extremely simple images. Figure 17 gives such an example. None of the methods in our experiments is able to produce nice results for this example, since the lack of edges makes the kernel estimation unreliable. However,

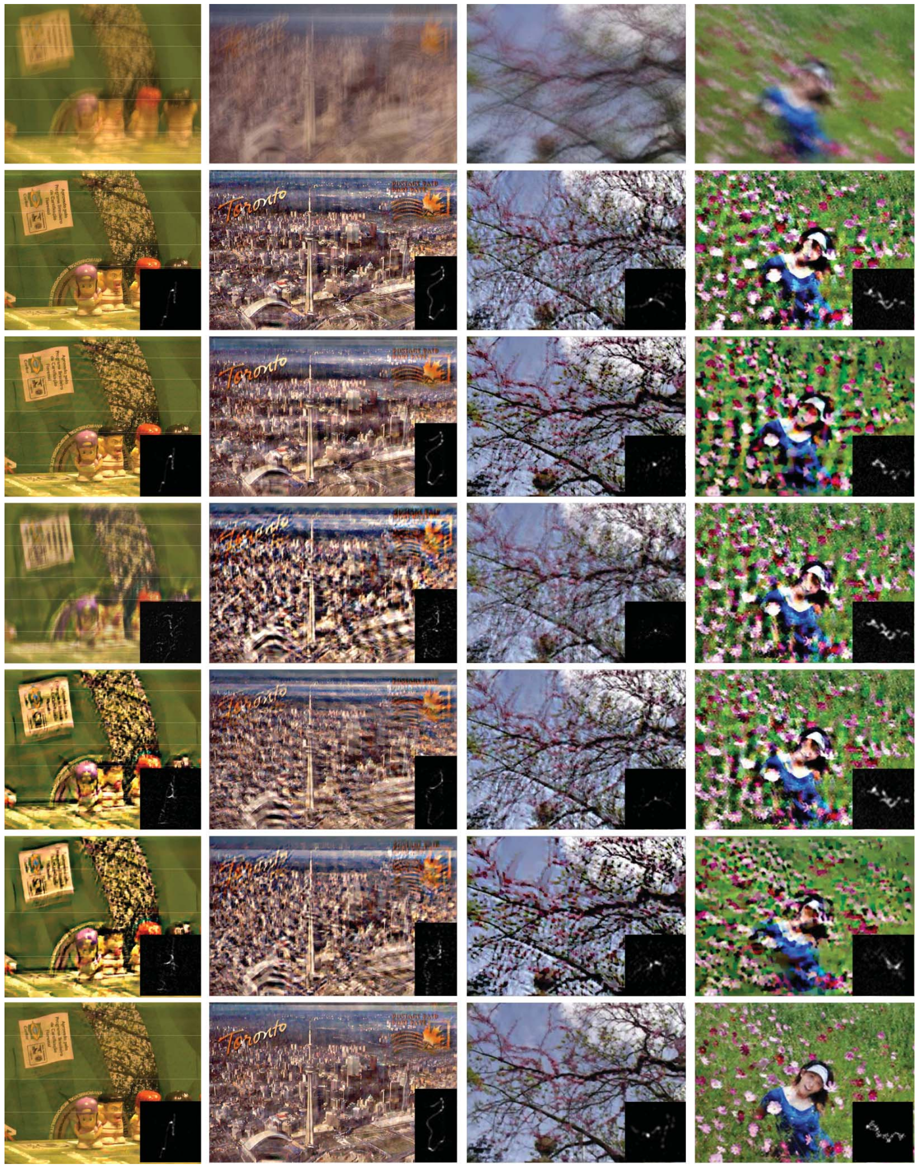

(a) (b) (c) (d)

Fig. 16. Comparison on four images with quite large kernels. From top to bottom are the blurred images, the results by Xu *et al.* [18], Cho *et al.* [17], Fergus *et al.* [9], Levin *et al.* [25], Krishnan *et al.* [24], and by our method. (a) and (b) Two images, which contain many large step edges. (c) and (d) Two images, which lack step edges.

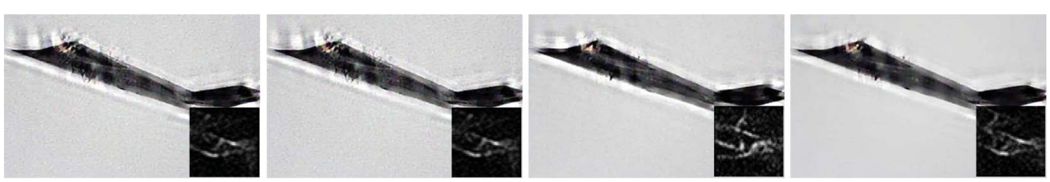

(a) (b) (c) (d)

Fig. 17. Results for the extremely simple image in Fig. 9(b). None of the methods in our comparison produces an accurate kernel. The results by (a) Fergus *et al.* [9], (b) Levin *et al.* [25], (c) Krishnan *et al.* [24], and (d) our result. The results by Cho *et al.* [17] and Xu *et al.* [18] are shown in Fig. 9(c) and (d).

this type of image accounts for less than 0.02% of the total images in ImageNet.

Also, like most other blind motion deblurring methods, we do not consider common photographic artifacts, such as over- and under-exposed regions, non-Gaussian noise and non-linear tone scale. Incorporating these factors into blind motion deblurring will be interesting to our future work.

VIII. Conclusion

Blind motion deblurring is a chronic inverse problem in the image processing community. This paper discusses a critical issue in current methods - their robustness to image diversity, which has been neglected for many years. In fact, this is a serious problem for some algorithms, although high quality results have been reported for experiments on a small number of standard testing data sets.

We conclude that the sources of the sensitivity to image diversity in many of the existing methods originate from the failure to handle edge variation and statistical variation. Further, we have revealed that using statistics adaptively is the key to enhancing the robustness. Based on this principle, NEAS is proposed as a novel blind motion deblurring method. Experiments on a large set of images have shown that it produces high-quality results.

References

[1] G. R. Ayers and J. C. Dainty, "Interative blind deconvolution method and its applications," *Opt. Lett.*, vol. 13, no. 7, pp. 547–549, 1988.

[2] A. K. Katsaggelos and K. T. Lay, "Maximum likelihood blur identification and image restoration using the EM algorithm," *IEEE Trans. Signal Process.*, vol. 39, no. 3, pp. 729–733, Mar. 1991.

[3] E. Thiebaut and J. M. Conan, "Strict a priori constraints for maximum-likelihood blind deconvolution," *J. Opt. Soc. Amer. A, Opt., Image Sci., Vis.*, vol. 12, no. 3, pp. 485–492, 1995.

[4] A. C. Likas and N. P. Galatsanos, "A variational approach for Bayesian blind image deconvolution," *IEEE Trans. Signal Process.*, vol. 52, no. 8, pp. 2222–2233, Aug. 2004.

[5] R. Molina, A. K. Katsaggelos, J. Abad, and J. Mateos, "A Bayesian approach to blind deconvolution based on Dirichlet distributions," in *Proc. Int. Conf. Acoust. Speech Signal Process.*, Apr. 1997, pp. 2809–2812.

[6] D. Kundur and D. Hatzinakos, "Blind image deconvolution," *IEEE Signal Process. Mag.*, vol. 13, no. 3, pp. 43–64, May 1996.

[7] T. F. Chan and J. Shen, *Theory and Computation of Variational Image Deblurring* (IMS Lecture Notes). Singapore: World Scientific, 2006.

[8] J. Cai, H. Ji, C. Liu, and Z. Shen, "Blind motion deblurring from a single image using sparse approximation," in *Proc. IEEE Conf. Comput. Vis. Pattern Recognit.*, Jun. 2009, pp. 104–111.

[9] R. Fergus, B. Singh, A. Hertzmann, S. T. Roweis, and W. T. Freeman, "Removing camera shake from a single photograph," *ACM Trans. Graph.*, vol. 25, no. 3, pp. 787–794, 2006.

[10] M. M. Bronstein, A. M. Bronstein, M. Zibulevsky, and Y. Y. Zeevi, "Blind deconvolution of images using optimal sparse representations," *IEEE Trans. Image Process.*, vol. 14, no. 6, pp. 726–736, Jun. 2005.

[11] N. Joshi, R. Szeliski, and D. Kriegman, "PSF estimation using sharp edge prediction," in *Proc. IEEE Conf. Comput. Vis. Pattern Recognit.*, Jun. 2008, pp. 1–8.

[12] A. Levin, "Blind motion deblurring using image statistics," in *Advances in Neural Information Processing Systems*, vol. 19. Cambridge, MA: MIT Press, 2006, pp. 841–848.

[13] J. Jia, "Single image motion deblurring using transparency," in *Proc. IEEE Conf. Comput. Vis. Pattern Recognit.*, Aug. 2007, pp. 1–8.

[14] J. W. Miskin and D. J. C. MacKay, "Ensemble learning for blind image separation and deconvolution," in *Advances in Independent Component Analysis*. New York: Academic, 2000.

[15] Q. Shan, W. Xiong, and J. Jia, "Rotational motion deblurring of a rigid object from a single image," in *Proc. IEEE Int. Conf. Comput. Vis.*, Oct. 2007, pp. 1–8.

[16] A. Levin, Y. Weiss, F. Durand, and W. T. Freeman, "Understanding and evaluating blind deconvolution algorithms," in *Proc. IEEE Int. Conf. Comput. Vis.*, Aug. 2009, pp. 1–8.

[17] S. Cho and S. Lee, "Fast motion deblurring," in *Proc. SIGGRAPH ASIA*, 2009, pp. 1–145.

[18] L. Xu and J. Jiaya, "Two-phase kernel estimation for robust motion deblurring," in *Proc. 11th Eur. Conf. Comput. Vis.*, 2010, pp. 1–14.

[19] J. Deng, W. Dong, R. Socher, L.-J. Li, K. Li, and L. Fei-Fei, "ImageNet: A large-scale hierarchical image database," in *Proc. IEEE Conf. Comput. Vis. Pattern Recognit.*, Jun. 2009, pp. 248–255.

[20] Q. Shan, J. Jia, and A. Agarwala, "High-quality motion deblurring from a single image," in *Proc. SIGGRAPH*, 2008, pp. 1–10.

[21] S. Harmeling, M. Hirsch, and B. Scholkopf, "Space-variant single-image blind deconvolution for removing camera shake," in *Advances in Neural Information Processing Systems*. Cambridge, MA: MIT Press, 2010.

[22] T. S. Cho, S. Paris, B. Freeman, and B. Horn, "Blur kernel estimation using the radon transform," in *Proc. IEEE Conf. Comput. Vis. Pattern Recognit.*, Mar. 2011, pp. 241–248.

[23] M. Hirsch, C. J. Schuler, S. Harmeling, and B. Scholkopf, "Fast removal of non-uniform camera shake," in *Proc. IEEE Int. Conf. Comput. Vis.*, Aug. 2011, pp. 1–8.

[24] D. Krishnan, T. Tay, and R. Fergus, "Blind deconvolution using a normalized sparsity measure," in *Proc. IEEE Conf. Comput. Vis. Pattern Recognit.*, Jun. 2011, pp. 233–240.

[25] A. Levin, Y. Weiss, F. Durand, and W. T. Freeman, "Efficient marginal likelihood optimization in blind deconvolution," in *Proc. IEEE Conf. Comput. Vis. Pattern Recognit.*, Jul. 2011, pp. 2657–2664.

[26] A. Levin, R. Fergus, F. Durand, and B. Freeman, "Image and depth from a conventional camera with a coded aperture," in *Proc. SIGGRAPH*, 2007, pp. 1–70.

[27] D. Krishnan and R. Fergus, "Fast image deconvolution using hyper-Laplacian priors," in *Advances in Neural Information Processing Systems*. Cambridge, MA: MIT Press, 2009.

[28] S. Roth and M. J. Black, "Fields of experts: A framework for learning image priors," in *Proc. IEEE Conf. Comput. Vis. Pattern Recognit.*, Jun. 2006, pp. 860–867.

[29] Y. Weiss and W. T. Freeman, "What makes a good model of natural images?" in *Proc. IEEE Conf. Comput. Vis. Pattern Recognit.*, Jun. 2007, pp. 1–8.

[30] O. Whyte, J. Sivic, A. Zisserman, and J. Ponce, "Non-uniform deblurring for shaken images," in *Proc. IEEE Conf. Comput. Vis. Pattern Recognit.*, Jun. 2010, pp. 491–498.

[31] G. Ankit, J. Neel, Z. Larry, C. Michael, and C. Brian, "Single image deblurring using motion density functions," in *Proc. 11th Eur. Conf. Comput. Vis.*, 2010, pp. 171–184.

[32] A. Koschan and M. Abidi, "Detection and classification of edges in color images," *IEEE Signal Process. Mag.*, vol. 22, no. 1, pp. 64–73, Jan. 2005.

[33] S. Roth and M. J. Black, "Steerable random fields," in *Proc. IEEE Int. Conf. Comput. Vis.*, Oct. 2007, pp. 1–8.

[34] B. Kris, P. Kristiaan, S. Johan, S. Johan, M. Bart, and V. Joos. (2010). *LS-SVMlab1.8* [Online]. Available: http:www.esat.kuleuven.ac.be/sista/lssvmlab

[35] L. Yuan, J. Sun, L. Quan, and H.-Y. Shum, "Image deblurring with blurred/noisy image pairs," *ACM Trans. Graph.*, vol. 26, no. 3, pp. 1–10, 2007.

Chao Wang received the B.S. degree from the Harbin Institute of Technology, Harbin, China, in 2001, the M.Sc. degree from Nanjing University, Nanjing, China, in 2004, and the Ph.D. degree from Tsinghua University, China, in 2010.

He was a Research Fellow of the Department of Computer Science and Technology, University of Bedfordshire, Luton, U.K. His current research interests include image processing and computer vision.

Yong Yue received the B.Sc. degree in mechanical engineering from Northeastern University, Shenyang, China, and the Ph.D. degree in CAD/CAM from Heriot-Watt University, Edinburgh, U.K.

He was a Design and Development Engineer in industry for eight years. He was a Post-Doctoral Researcher with the University of Nottingham, Nottingham, U.K., and a Project Manager with Cardiff University, Cardiff, U.K., before joining the University of Bedfordshire, Luton, U.K. He is currently the Head of the Department of Computer Science and Technology, University of Bedfordshire. His current research interests include computer graphics, mechatronics, and operating systems.

Feng Dong received the B.Sc., M.Sc., and Ph.D. degrees from Zhejiang University, Hangzhou, China.

He is a Professor of visual computing. He joined as CCGV from Brunel University, Middlesex, U.K., in September 2007. He became a member of academic staff with the State Key Lab of CAD and Computer Graphics, the leading computer graphics lab in China. His recent work has also developed new areas in visual analytics, pattern recognition, image-based rendering, and figure animation. His current research interests include computer graphics, medical visualization, and image processing.

Yubo Tao received the B.S. and Ph.D. degree in computer science and technology from Zhejiang University, Hangzhou, China, in 2003 and 2009, respectively.

He is currently a Post-Doctoral Researcher with the State Key Laboratory of CAD&CG, Zhejiang University. His current research interests include computational electromagnetic and scientific visualization.

Xiangyin Ma received the B.Sc. degree in mathematics from Nankai University, Tianjin, China, in 2003, and the Ph.D. in computer science from Peking University, Beijing, China, in 2009.

She has been a Lecturer with the Zhejiang University of Technology, Hangzhou, China, since July 2009, and as a Research Fellow with the University of Bedfordshire, Luton, U.K., from April 2011. Her current research interests include computer vision, computer graphics, and medical visualization.

Gordon Clapworthy joined the University of Bedfordshire, Luton, U.K., as the first Director of the Institute for Research in Applicable Computing, in 2003. He has had a wide-ranging career in research, covering projects in transonic aerodynamics, work with the Russian Academy of Sciences on space robots, investigations in clinical biomechanics with European partners in Belgium and Italy, and long-established work in computer graphics, particularly medical visualization.

Hai Lin received the B.Sc. and M.Sc. degrees in electrical engineering from Xidian University, Xi'an, China, in 1987 and 1990, respectively, and the Ph.D. degree in computer science from Zhejiang University, Hangzhou, China, in 2000.

He is currently a Professor of visual computing with the State Key Laboratory of CAD&CG, Zhejiang University. He is a Visiting Professor of the Department of Computing and Information Systems, University of Bedfordshire, Luton, U.K. His current research interests include computational electromagnetic, computer graphics, and scientific visualization.

Xujiong Ye received the Ph.D. degree from Zhejiang University, Hangzhou, China, in 1997.

She is currently a Reader with the School of Computer Science, University of Lincoln, Lincoln, U.K. From 1999 to 2002, she was a Researcher with the Engineering Department, Medical Vision Laboratory, University of Oxford, Oxford, U.K. From 2002 to 2012, she was a Senior Scientist with Medicsight Ltd., London, U.K., where she led advanced research and development in medical imaging. He has over 40 publications and four pending patents. Her current research interests include the area of image processing, computer vision, and medical imaging in general with a focus on computer-aided detection.